Engineered Science

RESEARCH PAPER

View Article Online

Polyelectrolyte Assisted Preparation of Nanocatalysts for CO_2 Methanation

Lei Liu,[1] Paul Bernazzani,[2] Wei Chu,[1] Shi-Zhong Luo,*[1] Bin Wang*[3] and Zhanhu Guo*[4]

The desire to form supported nanoparticles with fine-tuned size and distribution motivates the application of speciation-control of precursors. We propose to use a ternary metal ion/polyelectrolyte/oxide support hybrid as the means to generate a controlled precursor species. We first modify alumina with poly(acrylic acid), followed by nickel ion sorption to generate catalyst precursors. The precursors are then converted to catalysts used in CO_2 methanation. The parameters of polyelectrolyte incorporation are found to play a critical role in determining the resultant catalyst performances. The application of polyelectrolyte in assisting metal nanoparticle formation on oxide support emerges as a versatile, potentially universal, and industrially relevant approach to manufacturing heterogeneous catalysts..

Keywords: Polyelectrolyte/metal oxide hybrid; CO_2 methanation; Nickel nanoparticle catalyst

Received 18th April 2018, Accepted 15th May 2018

DOI: 10.30919/es8d637

1. Introduction

Large scale industrial operations such as hydrogenation, catalytic cracking, naphtha reforming, ethylene oxidation, and ammonia synthesis, to name a few, commonly use heterogeneous catalysts.[1] Market competition drives these industries to search for better performing catalysts, which has led to the development of an important class of heterogeneous catalysts involving nanoparticles of an active species supported on oxides having a high surface area.[2] Impregnation is a method applied throughout industry because it is a simple, economic, and usually reproducible way to form supported metal nanoparticle catalysts.[3] However, this method is not without pitfalls, some of which may lead to inconsistent performance.[4,5] One major issue concerns the possible absence of a specific interfacial binding mechanism, in which case the metal precursor species can migrate on the support surface during the treatments after adsorption causing inhomogeneous dispersions.[6] And, the support material surface contains irregularities in terms of exposed crystal facets, phases, and defect structures that will influence precursor adsorption.[6] To circumvent the inhomogeneously produced active phase, loading of pre-formed metal nanoparticles onto support has been attempted. But this approach suffers from only being capable to deposit relatively small amounts of nanoparticles,[7,8] as well as the irreproducible nature of the nanoparticle preparation.[5] In addition, remaining organic ligands binding to the nanoparticles during the preparation can result in relatively poor catalytic properties.[9] These issues generate inconsistencies in nanoparticle size, composition, distribution and performance. An imperative need is to create supported catalysts with consistently uniform distribution of the active phases that provide improved activity.

Current industrial efforts center on improvements for the in situ generation of the active nanoparticles. Studies show that incorporation of specific metal ions during the preparation can provide better distributed nanoparticles.[10,11] One approach involves using silane molecules bearing functional groups such as amines to modify the support surface with coordination sites for the uniformly adsorption of metal precursor ions.[12,13] This method has resulted in catalysts with metal nanoparticles that are relatively uniform in size and distribution. However, the stringent moisture sensitivity of silanes limits the industrial applicability potentials. A few studies have explored the utilization of metal-polyelectrolyte complexes in assisting the synthesis of metal nanoparticles on oxide support. The layer-by-layer self assembly method was employed to prepare a metal-polyelectrolyte complex layer wrapping around alumina particles.[14,15] Following reduction this wrapping helped to obtain well dispersed metal nanoparticles with a narrow size distribution. Yet, the remaining polyelectrolytes in the catalyst systems seemed to limit the catalytic activity, similar to that reported by Rinaldi et al.[9]

Intrigued by the employment of metal ion-polyelectrolyte complexes in assisting nanoparticle formation on catalyst support,[16] we first studied the interaction between a polyelectrolyte, poly(acrylic acid)

---

[1] *School of Chemical Engineering, Sichuan University, Chengdu, Sichuan 610065, China. E-mail: luosz@scu.edu.cn*

[2] *Department of Chemistry and Biochemistry, Lamar University, Beaumont, Texas 77710, USA*

[3] *Engineered Multifunctional Composites (EMC) Nanotech, Knoxville, TN 37934, USA. E-mail: scienceemc@emcnanotech.com*

[4] *Integrated Composites Laboratory (ICL), Department of Chemical and Biomolecular Engineering, University of Tennessee, Knoxville, TN 37996, USA. E-mail: zguo10@utk.edu*

(PAA), and alumina.[17] Using the insight provided in the study, we set out to produce proof-of-concept catalyst samples based on the use of PAA as a coordination agent for the efficient formation of nanoparticles on alumina. PAA was used to form composite with carbon nanotubes, followed by adsorption of Pt ions.[18] Reduction afforded Pt nanoparticles supported on carbon nanotubes that showed advantageous catalytic performance than samples without PAA. The dispersion effect of polymer chains was illustrated. We, as others,[19] are interested in CO_2 conversion to useful bulk products, and use as the reporter reaction of CO_2 methanation[20] to test the proposed novel catalyst fabrication method. Significant kinetic barriers are associated with the eight-electron reduction of CO_2 methanation.[21] Systems based on nickel nanoparticles supported on alumina, usually prepared via the impregnation method, have been the preferred industrial catalysts for this reaction.[22] Hereby, we prepare alumina-supported Ni catalysts as the proof-of-concept example to test the effects of polyelectrolyte infiltration on nanoparticle formation, and catalytic behavior of the nanoparticles.

2. Experimental section

2.1. Materials.

γ-Al_2O_3 with 40-60 mesh (Tianjin Kemiou Chemicals Co.) was heated at 500 °C in air for 3 h for activation. Poly(acrylic acid) with M_W 3 000 g mol^{-1} was acquired from Shanghai Aladin Reagents Co in 50 wt% solution. $Ni(NO_3)_2$, NaOH, HCl, and $NaNO_3$ were analytical reagents. Water with conductivity $\leq$10 μS cm^{-1} was used throughout the experiments.

2.2. Preparation of supported Ni catalysts

The catalyst preparation was carried out in two steps. The first step was to prepare the binary PAA-Al_2O_3 hybrids, fabricated according to the method reported in our previous study.[17] Briefly, 100-mL PAA solution was added with 3.0 g freshly activated alumina. The mixture was gently stirred at room temperature (unless indicated otherwise) for $\geq$12 h, then filtered and rinsed with small portions of water. The solid was collected and dried at 110 °C in air for $\geq$12 h. The samples prepared with PAA pH at 4.0, 5.5, 5.5 plus 0.2 M $NaNO_3$, and 5.5 at 100 °C were denoted as Al_4, $Al_{5.5}$, $Al_{5.5\text{-s}}$, and $Al_{5.5\text{-t}}$, respectively, while the control alumina was named Al.

The second step was to use the hybrids as precursors to prepare the ternary Ni^{2+}-PAA-Al_2O_3 composites via the conventional incipient wetness impregnation method. After drying the composites at 110 °C overnight, the ternary samples were calcined in air for 5 h to produce supported nickel nanoparticle catalysts. The formed catalysts 5Ni/Al_x were named according to the binary PAA-Al_2O_3 hybrid preparation condition (calcined at 450 °C), and 15Ni/Al_y according to the calcination temperature (350 or 450 °C). 1) 5Ni/Al, formed by adding $Ni(NO_3)_2$ solution (5% Ni by weight) to Al. 2) 5Ni/Al_4, formed by adding $Ni(NO_3)_2$ solution (5% Ni by weight) to Al_4, the solution pH lower than the pK_a of PAA. At this pH, the resulting PAA adsorbed on alumina would be in molecular form. 3) 5Ni/$Al_{5.5}$, formed by adding $Ni(NO_3)_2$ solution (5% Ni by weight) to $Al_{5.5}$, the solution pH higher than the pK_a of PAA. At this pH, the resulting PAA adsorbed on alumina would contain ionic carboxylic acid groups. 4) 5Ni/$Al_{5.5\text{-s}}$, formed by adding $Ni(NO_3)_2$ solution (5% Ni by weight) to $Al_{5.5\text{-s}}$. 5) 5Ni/$Al_{5.5\text{-t}}$, formed by adding $Ni(NO_3)_2$ solution (5% Ni by weight) to $Al_{5.5\text{-t}}$. 6) 15Ni/Al, formed by adding $Ni(NO_3)_2$ solution (15% Ni by weight) to Al and calcined at 450 °C. 7) 15Ni/Al_{350}, formed by adding $Ni(NO_3)_2$ solution (15% Ni by weight) to $Al_{5.5}$ and calcined at 350 °C. 8) 15Ni/Al_{450}, formed by adding $Ni(NO_3)_2$ solution (15% Ni by weight) to $Al_{5.5}$ and calcined at 450 °C.

2.3. Characterization of supported Ni catalysts

Room temperature Fourier transform infrared (FT-IR) was performed on a Bruker Tensor 27 Fourier transform spectrometer. The specific surface areas, total pore volumes, and average pore diameters were determined from the nitrogen adsorption-desorption isotherms at -196 °C, which were measured using an automated surface area and pore size analyzer (Quadrasorb SI apparatus). Before each measurement, the samples were degassed in vacuum at 300 °C for 3 h. Specific surface areas of samples were calculated by the Brunauer-Emmett-Teller (BET) method, and the pore size distribution and average pore diameter were determined according to the Barrett-Joyner-Halenda (BJH) method applied to desorption isotherms. X-ray diffraction (XRD) patterns were acquired on a Philips X'pert PRO diffractometer using Cu Kα radiation (45 kV, 50 mA). Samples were scanned between 10 and 80° (2θ) at a scan step size of 0.03° and scan time constant of 2 s per step. The Ni crystallite size (d_{XRD}) was determined by X-ray line broadening analysis according to the Scherrer method. Inductively coupled plasma atomic emission spectrometry (ICP AES) was performed on TJA IRIS. The morphologies of the samples were recorded using transmission electron microscopy (TEM) on a JEOL TEM 2010 operated at 120.0 kV. CO_2 conversion/CH_4 production thermodynamic limit was obtained by a simulation program (Aspen Plus).[23] The calculations were carried out by using the Rigorous equilibrium reactor, which was based on stoichiometric approach and thermodynamic equilibrium. The chosen method was PENG-ROB. The feed and reactor conditions were similar to the actual reaction conditions. Activation energy values were acquired following a literature method.[24] Turnover number (TON) was calculated according to a literature method.[25]

2.4. Gas chromatography experiments

A continuous flow fixed-bed reactor operated at 0.1 MPa was used to test catalytic performance of the catalysts. Feed and product gas analysis was performed in a gas chromatograph (GC-1690, Hangzhou Kexiao Instrument) equipped with a thermal conductivity detector. For each run, about 200 mg of catalyst was loaded into a quartz reactor and reduced in situ under a continuous flow of H_2 at the rate of 40 mL min^{-1} at 600 °C for 1 h at a heating rate of 10 °C min^{-1}, normal pressure of one bar, and GHSV of 15000 mL h^{-1} $g_{cat}{}^{-1}$. The catalyst was cooled to 100 °C, and a CO_2 flow of 10 mL min^{-1} was added to the H_2 flow. The catalytic CO_2 conversion reaction was carried out in the temperature range 300-380 °C with a reactant flow rate of 50 mL min^{-1} of H_2/CO_2 (4:1) mixture. The reaction was equilibrated at each temperature point for at least 30 min to provide gas sample for GC analysis. The temperature points used were 300, 320, 340, 360, and 380 °C.

Temperature programmed reduction (TPR) analysis was conducted on the same setup for catalytic performance to determine the reducibility of the catalysts. About 50 mg of catalyst was placed in the quartz reactor and the temperature was raised from 100 to 800 °C at a heating rate of 10 °C min^{-1} under a 5% H_2/N_2 flow stream of 30 mL min^{-1}. The amount of hydrogen consumed was determined online using a gas chromatograph (SC-200, Chongqing Chuanyi Jiuchang) equipped with a thermal conductivity detector.

2.5. Mass spectrometry experiments

The in situ temperature-programmed surface reaction (TPSR) of CH_4 and CO was achieved with a fixed-bed reactor. The catalyst was first reduced under a hydrogen flow (40 mL min^{-1}) at 600 °C for 1 h. After cooled to 50 °C, a flow of 50 mL min^{-1} of H_2/CO_2 (4:1) was used. The temperature of the reactor was raised linearly from 100 to 700 °C at a rate of 10 °C min^{-1} with GHSV of 15000 mL h^{-1} g_{cat}^{-1}. The products of reaction were analyzed on-line by a mass spectrometer (QIC-20, Hiden Analytical).

Transient CH_4 production was conducted under conditions similar to that of TPSR. After reduction and cooling, a flow of 50 mL min^{-1} of H_2/CO_2 (4:1) was used and the temperature was raised to 340 °C at 5 °C min^{-1}. The outlet gases were analyzed by a mass spectrometer: for panel A, it initiated when CO_2 gas flow was stopped; and for panel B, the starting point was when H_2 gas flow was stopped for 5Ni/Al$_{5.5}$.

2.6. Modified calculation of CO_2 methanation

The catalytic conversion of CO_2 to CH_4 can be expressed by using a simplified mechanism as schematically represented in Scheme 1 and can be written

$$8H_2 \leftrightarrow 16H \tag{1}$$

$$2CO_2 + 2H \leftrightarrow 2HCOO^- \tag{2}$$

$$2HCOO^- + 2H \leftrightarrow 2H_2O + 2CO \tag{3}$$

$$2CO + 12H \leftrightarrow 2CH_4 + 2H_2O \tag{4}$$

Scheme 1 Representation of CO_2 methanation catalyzed by Al_2O_3 supported Ni nanocatalyst.

The mechanism also involves adhesions to either Ni or the substrate as two different binding sites.[26] Step (2) is the rate determining step. Reaction (1) is so fast that H is in equilibrium with H_2, while steps (3) and (4) are fast enough that the surface coverage of the compounds involved is negligible.

The kinetics of the catalytic system can be studied by analyzing the transient production of CH_4, shown to be related to the partial pressures of the reactants:

$$-\frac{dP_{CO_2}}{dt} = \frac{dP_{CH_4}}{dt} = K P_{CO_2} P_{H_2}^{1/2} \tag{5}$$

where K is a product of rate constants.

Here, the Al_2O_3 layer (grey) represents the surfaces of mesoporous alumina, including both inner and outer surfaces. The inner surface of the alumina exists either as amorphous or in a linear fashion, cf. TEM images, Fig. 2.

3. Results and discussion

3.1. Catalyst characterization of 5% Ni-loading samples

The catalysts were prepared using our previously produced PAA-alumina hybrids[17] and incorporating Ni ion via the incipient wetness impregnation method. Upon addition of metal ion to the PAA-alumina hybrid, the infrared of the ternary Ni^{2+}-PAA-alumina showed a strong peak around 1380 cm^{-1} (shown as the arrow), indicating the coordination between the divalent ions and carboxylate groups (Fig. 1).[27] The ensuing catalyst preparation followed typical industrial procedures in which calcination would have decomposed the polyelectrolyte ligands. Exemplary transmission electron microscope (TEM) images of four H_2-reduced samples of 5Ni/Al, 5Ni/Al$_4$, 5Ni/Al$_{5.5}$, and 5Ni/A$_{5.5\text{-}s}$ are displayed in Fig. 2. Sample 5Ni/Al$_{5.5\text{-}t}$ had similar characteristics to that of 5Ni/Al$_{5.5}$ and data not shown here. Sample 5Ni/Al$_{5.5}$ maintained the finest particle size of 3.19 nm and the narrowest distribution of ±1.17 nm. The nanoparticles were also relatively evenly dispersed on the support in this sample. In contrast, samples 5Ni/Al, 5Ni/Al$_4$, and 5Ni/Al$_{5.5\text{-}s}$ all presented images of

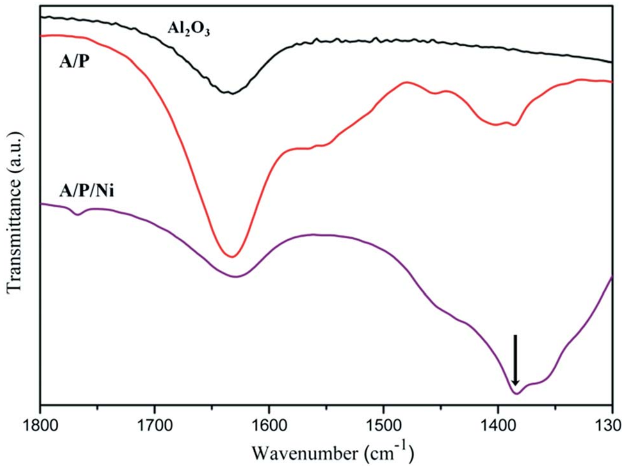

Fig. 1 FT-IR spectra of alumina, PAA/alumina, and Ni/PAA/alumina.

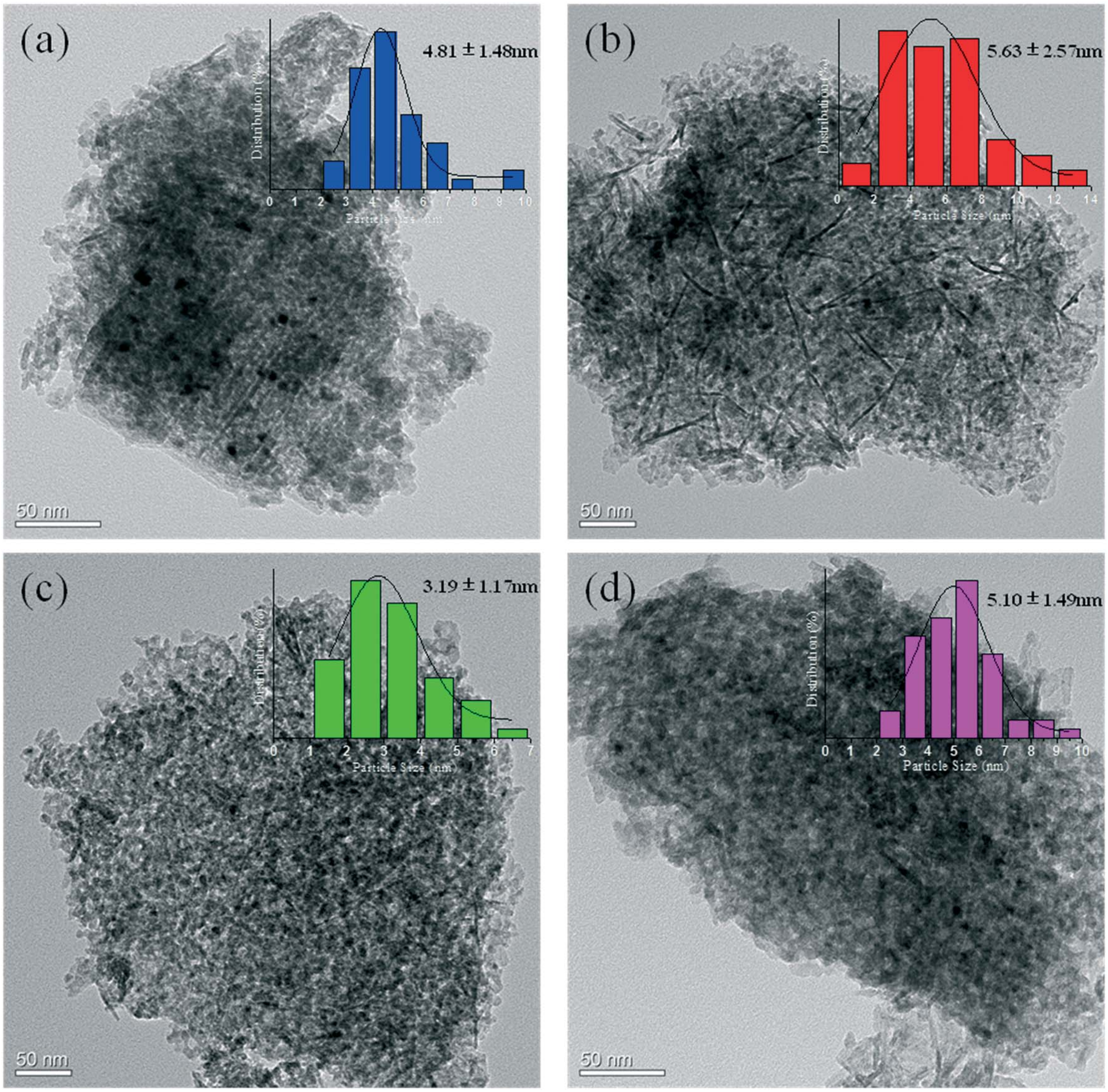

Fig. 2 TEM of (a) Ni/Al, (b) Ni/Al_4, (c) $Ni/Al_{5.5}$, and (d) $Ni/Al_{5.5\text{-}s}$. Black dots are nickel nanoparticles while the dark gray mesh-like matter is alumina. The nanoparticle size and distribution are shown as insets.

larger particle sizes and wider distributions, although all differences between the four samples are within one standard deviation.

The characteristics of the four catalyst samples are presented in Table 1. The surface area and pore volume values of the catalyst samples are lower than that of the precursor hybrids,[17] indicating effective nickel incorporation. The powder X-ray diffraction (XRD) measurements were performed and all peaks were identified with JCPDS files as shown in Fig. 3. The nanoparticle sizes calculated from XRD data (Table 1) were slightly greater than the data acquired from TEM data, a phenomenon observed in a literature report in which Co was

Table 1 Physicochemical and catalytic characteristics of catalyst samples.

Sample	***S.A.*** **(m^2g^{-1})**	**Pore *V*** **(cm^3g^{-1})**	**Pore ϕ** **(nm)**	**Particle ϕ** **(nm)[a]**	**Ni** **(wt%)[b]**	**E_a** **(kJ mol^{-1})**	**TON[c]** **(10^2 s^{-1})**
5Ni/Al	154.0	0.3379	8.779	7.43	5.11	65.26	5.8
$5Ni/Al_4$	163.9	0.3642	9.071	8.33	5.03	70.34	4.6
$5Ni/Al_{5.5}$	157.1	0.3743	9.530	5.67	5.17	55.91	6.6
$5Ni/Al_{5.5\text{-}s}$	144.5	0. 3606	9.983	8.00	4.98	66.95	6.9
15Ni/Al	115.3	0.3195	11.08	13.30	-	58.64	5.8
$15Ni/Al_{450}$	109.2	0.2809	11.43	12.33	-	54.01	6.4
$15Ni/Al_{350}$	110.8	0.2948	10.64	8.80	-	31.33	5.4

[a] determined with XRD using the Scherrer equation [b] determined with ICP AES [c] determined at 340 °C

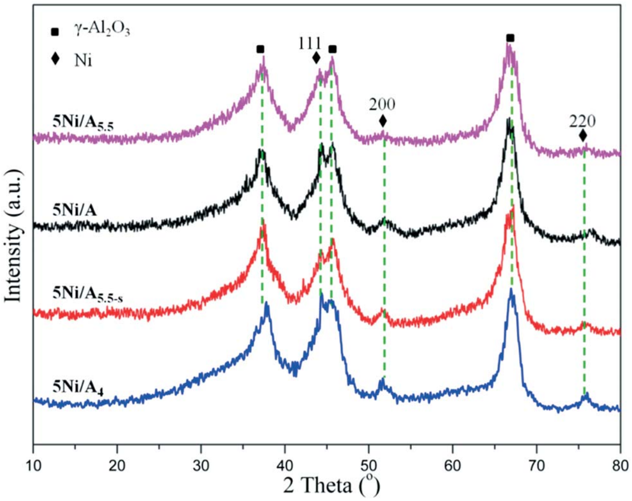

Fig. 3 X-ray diffraction peaks of four 5% Ni-loading catalyst samples.

incorporated onto γ-alumina as Fischer-Tropsch catalysts.[28] These four samples contained Ni particles with diameters smaller than the alumina pore diameter, implying incorporation of the active phase residing inside the support pores.[28] The nickel contents of the samples are revealed by inductively coupled plasma atomic emission spectrometry (ICP AES) analysis (Table 1), manifesting that all four samples had around 5% nickel loading. It is obvious that 5Ni/Al$_{5.5}$ had smaller nanoparticle size, even though it had about the same amount of Ni as did the other three samples. Therefore, the nanoparticle dispersion in sample 5Ni/Al$_{5.5}$ was the finest among the four samples. It is intriguing to find how the varied nanoparticle size and dispersion patterns affected the individual catalytic performance.

3.2. CO_2 methanation performance of 5% Ni loading samples

Examination of the catalytic CO_2 methanation was conducted over a temperature range of 300-380 °C. Fig. 4 displays the triplicate CH_4 average yield versus temperature for four catalyst samples with 5% Ni loading. Across the temperature range the sample catalysts performed similarly, producing more CH_4 at higher temperatures. The control 5Ni/Al catalyst had an average performance with a yield of CH_4 of 65.7% at 380 °C. In comparison, sample 5Ni/Al$_{5.5}$ performed significantly better with a yield of 76.5% at this temperature. Sample 5Ni/Al$_{5.5\text{-t}}$ had a CH_4 formation yield of 80.8% at 380 °C, the highest among the five samples with 5% Ni loading (data not shown in Fig. 4). According to the reptation motion model,[29,30] polymer infiltration of confined media proceeds further at higher temperatures, covering more support surface. In sample 5Ni/Al$_{5.5\text{-t}}$, more PAA molecules on alumina could coordinate to more nickel ions, consequently formed more nanoparticles which showed high catalytic activity. The two other samples performed either close to the control (63.3% for 5Ni/Al$_{5.5\text{-s}}$), or in the case of 5Ni/Al$_4$, worse with a yield of 55.3%. Evaluation of the activation energies (Table 1) are obtained with the Ni/Al$_{5.5}$ showing a significantly lower value compared to the others, which correlates well with their respective catalytic activity. We also calculate the turnover number (TON) of each sample at 340 °C (Table 1). The TON value of sample 5Ni/A$_{5.5}$ is higher than that of both 5Ni/Al and 5Ni/Al$_4$, only slightly lower than that of 5Ni/Al$_{5.5\text{-s}}$, possibly due to coexistence of various Ni crystal phases within individual particles. The TON values of the catalysts presented here are in the same range of the 1% Ru catalyst prepared via the impregnation method in ref [25]. The variations in catalytic activities when PAA was used at different conditions lead us to investigate the thermodynamic and kinetic properties of the catalysts.

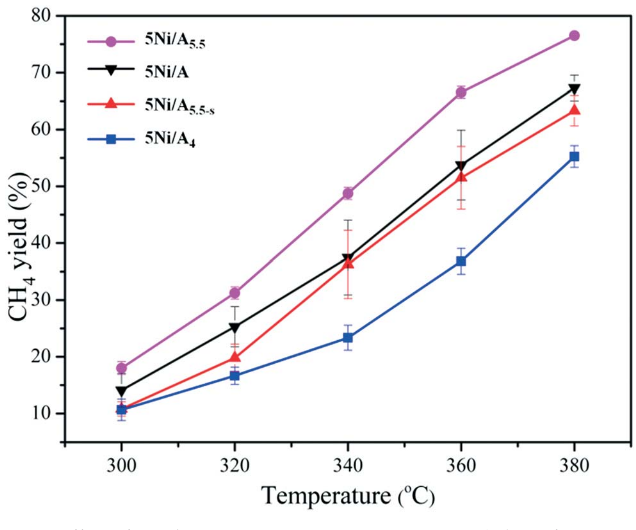

Fig. 4 Effect of reaction temperature (300-380 °C) on catalytic performance of 5% Ni-loading catalyst samples.

3.3. Temperature-programmed surface reaction (TPSR)

Gas phase reactions occur at the catalyst surface, so surface adsorption of key intermediates may affect catalyst performance. Because the stability of adsorbed species is determined by thermodynamic issues, temperature-programmed surface reaction (TPSR) experiments were carried out. The CH_4 and CO formation curves are presented in Fig. 5 with the curves of CO_2 consumption shown as an inset. The formation of CH_4 reached a maximum at temperatures between

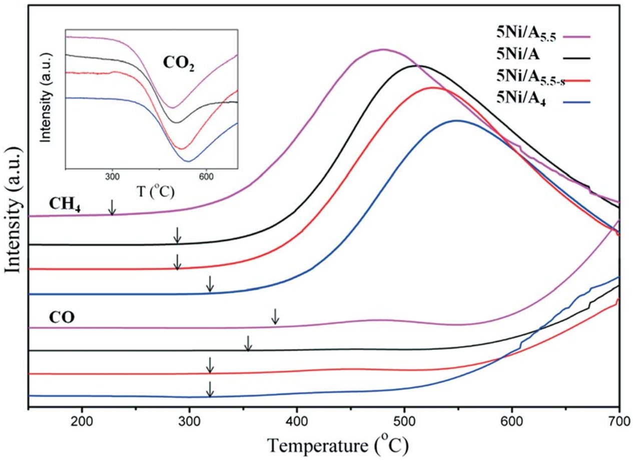

Fig. 5 CH_4-TPSR and CO-TPSR profiles of catalyst samples, changes of CO_2 signals with temperature shown as inset. Arrows indicate the CH_4 and CO activation temperatures.

475 and 550 °C depending on the nature of the catalyst, with the peak CH_4 formation for $5Ni/Al_{5.5}$ being at the lowest temperature (478 °C), while the temperatures for the peak CH_4 formation for other three samples were higher than 500 °C. The trend follows the activation energy values previously determined. For all samples, the formation of CH_4 decreased once higher temperatures were reached. As expected, the TPSR traces of CO_2 decreased in a pattern corresponding with the formation of CH_4. CO was detected at temperatures higher than CH_4 activation, suggesting its weaker carbon competing capability on these catalysts. Catalyst $5Ni/Al_{5.5}$ had the highest CO activation temperature, representing the best CH_4 selectivity amongst the four samples. CO was formed in significant amounts only at higher temperatures suggesting desorption of the material from the catalyst in combination with consumption of adsorbed carbon species by CO_2.[31]

3.4. Temperature-programmed H_2 reduction (TPR)

To evaluate the PAA influence on the catalyst performance, the temperature-programmed H_2 reduction (TPR) for the different nickel nanoparticle formation patterns of the four samples are plotted, along with the simulated area percentages of each sample (Fig. 6). Each sample showed three reduction peaks that represented three nickel species[32,33:] α-NiO, β-NiO, and γ-NiO. Type α-NiO is easily reduced to form aggregated nanoparticles that contribute insignificantly to the catalytic activity. The nickel nanoparticles formed by reducing β-NiO are the fine ones that constitute the majority of active catalytic sites, while type γ-NiO is the less reducible in the Al-rich phase that is prone to form the inactive spinel $NiAl_2O_4$. The TPR results show that $5Ni/Al_{5.5}$ had the highest percentage of β-NiO, leading to higher catalytic activity after reduction. $5Ni/Al_4$, on the other hand, had the highest γ-NiO content that could not be readily reduced to form active nickel nanoparticles. The reason why infiltrated PAA assisted the formation of β-NiO phase may be interpreted that the PAA layer provided a platform for Ni^{2+} sorption onto alumina surface. With the help of the platform, a significant portion of Ni ions maintained an advantageous distance from the —Al—O—Al— surface. During the calcination, these ions were prone to form the β-NiO phase.

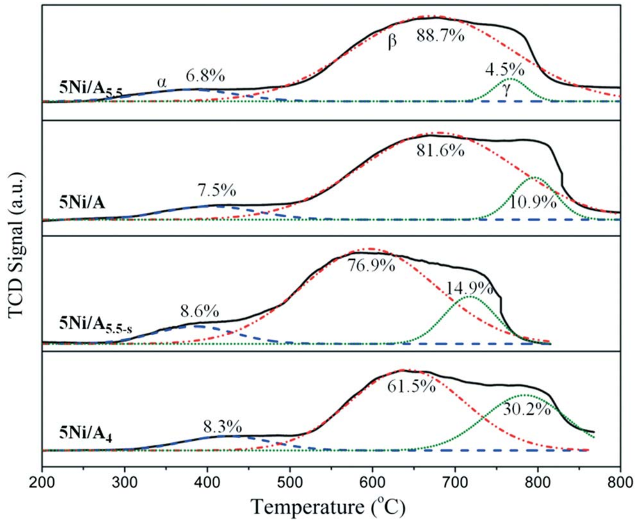

Fig. 6 TPR profiles of four 5% Ni-loading catalyst samples.

3.5. Transient CH_4 production

According to Equation (5), one assumes that H_2 and the intermediates do not compete for the binding sites on the catalyst which is valid at lower pressures. The assumption seems to hold for the data presented in Fig. 7 where the evolution of the formation of CH_4 was presented when the pressure of CO_2 was removed from the reaction, panel A or when the pressure of H_2 was removed, panel B. Under the former circumstances, the amount of CH_4 continued to be produced for a longer period of time for sample $5Ni/Al_{5.5}$, suggesting an improved binding between catalyst and all reagents and intermediates. This result is supported by the observed continued increase in CH_4 formation as H_2 was removed from the reaction vessel. We note that the catalytic activity of the 5Ni/Al sample behaved in line with literature[34] and is not presented here.

3.6. Enhanced CH_4 methanation activities with higher Ni-loading

Our hypothesis implies that infiltrated polyelectrolyte molecules can coordinate with metal ions to form the speciation-controlled metal ion-polyelectrolyte-support ternary precursor. This precursor is advantageous for the generation of nanoparticles with fine size and narrow distribution. To test the validity of our hypothesis, we continued the preparation of Ni/Al samples with better CO_2 methanation performance. This reaction can achieve a ~100% CH_4 yield at 160 °C with a Ru/TiO_2 system.[25] For catalyst systems with transition metals as the active phase, modification of the support oxides helps afford catalysts that show CH_4 yields close to the thermodynamic limits at temperatures above 300 °C.[35–37] Using commercially available oxide support materials and nickel contents ≥10%, similarly high catalytic performances have been reported.[38,39] It seems that high Ni loadings lead to better CO_2 methanation activities.

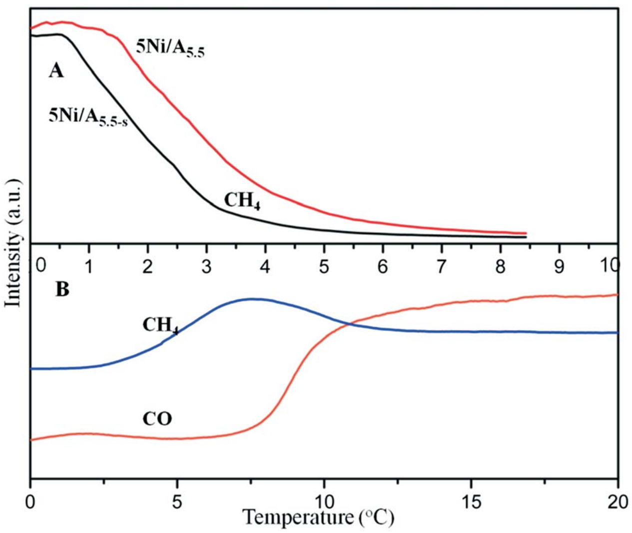

Fig. 7 Changes of outlet partial pressure of CH_4 for Ni/Al_i and $Ni/Al_{i\text{-}s}$ (A); Changes of outlet partial pressures of CH_4 and CO for Ni/Al_i (B).

Therefore, we prepared samples with 15% Ni and tested the catalytic performance. To further circumvent the potential sintering when heating the samples in air,[27] a lower calcination of 350 °C was also tested.

Similar to the situation with 5% Ni loading, adsorbed PAA helped form finer Ni particles when the two 15% Ni loading samples 15Ni/Al and 15Ni/Al_{450} are compared (Table 1). Meanwhile, the lower calcination temperature seemed to induce smaller Ni nanoparticles by comparing the Ni nanoparticle diameters of 15Ni/Al_{450} and 15Ni/Al_{350}. As in the case of 5% Ni loading samples, the Ni particle diameters of the 15% Ni loading samples are within the range of the alumina support pore diameter, indicating formation of Ni particles inside the support pores.[28]

The catalytic activities of the 15% Ni loaded samples are shown in Fig. 8. The control sample 15Ni/Al had a CH_4 yield of 81.5% at 380 °C, up 15.8% compared to 5Ni/Al. When incorporated with PAA and calcined at 450 °C, sample 15Ni/Al_{450} registered a CH_4 yield of 85.5%. Sample 15Ni/Al_{350}, calcined at 350 °C, exhibited a value of 87.4%, almost equal to the thermodynamic limit value of 87.6% at 380 °C (Table 2). Activation energy data present a similar trend among the three samples (Table 1), i.e., 15Ni/Al_{350} rendered the lowest value among all samples (including those with 5% Ni-loading). The TON values of the three 15%-Ni samples appear non-conclusive. It is known that CO_2 adsorption and dissociation are structure-sensitive on Ni surface.[40] Considering the large quantity of Ni loaded, it is possible that different crystalline phases coexist in all samples that make the distinction less likely. By increasing the Ni loading to 15%, the catalysts prepared from PAA-adsorbed precursors featured high catalytic CO_2 methanation activity. Further improvement of the catalyst performance is feasible, especially via the incorporation of metallic promoters.[32–34]

Table 2 CH_4 yields (%) of catalyst samples and the corresponding thermodynamic equilibrium values at selected temperatures.

Sample	300 °C	320 °C	340 °C	360 °C	380 °C
5Ni/Al	12.0	22.8	32.8	49.4	65.7
5Ni/Al_4	10.7	16.7	23.4	36.8	55.3
5Ni/$Al_{5.5}$	18.0	31.3	48.8	66.6	76.5
5Ni/$Al_{5.5\text{-}s}$	10.8	19.8	36.3	51.5	63.3
5Ni/$Al_{5.5\text{-}t}$	19.3	31.1	56.7	69.0	80.8
15Ni/Al	18.8	33.3	55.1	74.1	81.5
15Ni/Al_{450}	20.4	40.5	65.8	79.5	85.5
15Ni/Al_{350}	37.8	62.3	77.4	84.4	87.4
therm. eq.	95.0	93.5	91.8	89.8	87.6

3.7. Influence of polyelectrolyte infiltration on catalyst performance

Our investigation suggests that catalytic performances of the samples can be linked to their individual microstructures and chemical compositions, while these properties are influenced by precursor PAA infiltration. Scheme 2 summarizes our explanation of the chain of effects. The blue-grey represents the alumina phase not exposed in a surface, while the silver-grey represents the exposed surface area containing a channel which was not effectively covered by simple nickel deposition such as in 5Ni/Al. PAA polymer chains are represented by the red lines, Ni^{2+} ions by lavender dots, and Ni particles by black dots. When PAA was used at a pH > pK_a, polymer side chains were mostly in ionic form which resulted in the expansion of the random coils in solution. As this material was deposited on the alumina oxide surface, the stretched polymer main chains infiltrated the oxide pores more efficiently to form a partial layer on the channel surface (Scheme 2a). During the ensuing ion sorption, nickel ions were coordinated to the ionized carboxylic acid groups and became evenly immobilized related to underneath oxide surface (Scheme 2b). The successive nanoparticle nucleation and growth within the polymer matrix (albeit itself was eventually burnt off) were more restrained. Thereafter, the nickel nanoparticle size, size distribution, and dispersion were fine and narrow (Scheme 2c). In addition, the ionic PAA side chains interacted with nickel ions in such a way as to promote the formation of the more reactive β-NiO

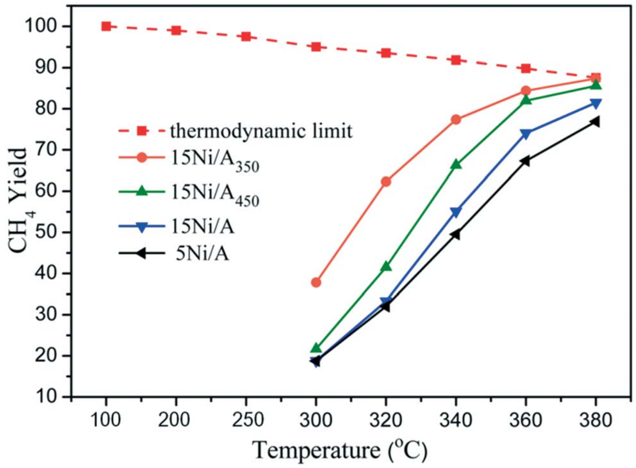

Fig. 8 Effect of reaction temperature (300-380 °C) on catalytic performance of 15% Ni-loading catalyst samples.

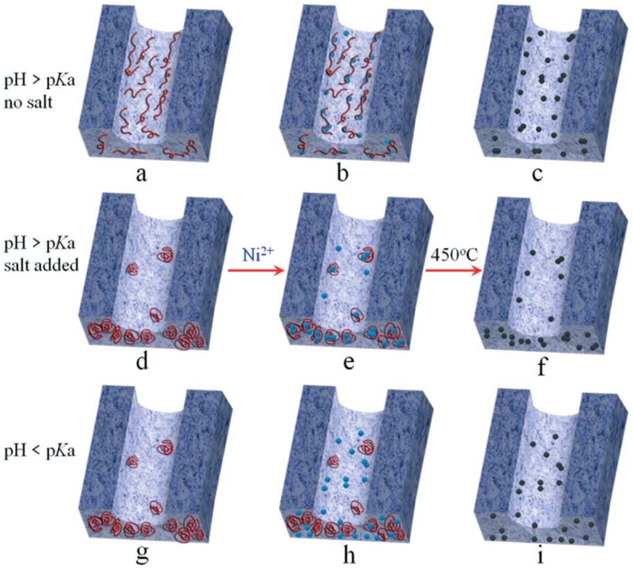

Scheme 2 Illustration of Ni nanoparticle formation on PAA-adsorbed alumina.

phase during calcination, even though the mechanism of this behaviour is not uncovered yet. If PAA was kept at a pH $> pK_a$ but the system was in the presence of other ions, the random coils of the polymer were not expanded due to the screening effect, and the channels of alumina substrate were not efficiently covered (Scheme 2d). As nickel was deposited in such channels, more Ni^{2+} ions were coordinated with PAA coils (Scheme 2e). After calcination, some nickel residing within PAA coils was removed from the catalyst leading to a lower Ni content in this sample (Scheme 2f). When PAA was used at a pH $< pK_a$, random coils of polymer were more compact because the side chains participated in more intramolecular hydrogen bonding. When alumina was pre-adsorbed with this PAA, the chains failed to cover the surface of channel (Scheme 2g). During the ion loading, the non-coordinating PAA chains competed for adsorption sites on alumina surface with Ni^{2+}, resulting in nickel deposition inferior to that of the system without using PAA (Scheme 2h). Following calcination the nickel nanoparticle size, size distribution, and dispersion were large (Scheme 2i). In addition, the absence of ionic side chains failed to promote the formation of the β-NiO phase. Thus 5Ni/Al_4 behaved poorly even compared to 5Ni/Al. For the PAA-treated samples, the polymer infiltration pattern translates into the Ni particle size and distribution, which in turn determine the catalytic activity of each sample. Our related study demonstrates that only PAA with small enough molecular weights could infiltrate the alumina pores to enhance the catalyst microstructure thus better CO_2 methanation performance.[41]

4. Conclusions

In summary, we propose a new paradigm in heterogeneous catalyst preparation via the incorporation of metal-polyelectrolyte-support complexes as the speciation-controlled active phase precursors. In the composite, infiltrated polymer chains would cover the high energy portions of the oxide surface first, coincident with the sites that would have interacted strongly with metal ions. The following metal ion adsorption thus took place less on the strong-interaction sites. This scenario led to the decreased formation of γ-NiO, the species not easily reduced. Here, polymer chains connected nickel ions and alumina surface sites in a way that functioned uniquely in the ensuing treatments. With the connection, nickel species less likely roamed above the oxide surface freely to form α-NiO, nor did it interact strongly with alumina like that of γ-NiO. Polyelectrolytes anchored nickel species to a certain degree that favored the formation of β-NiO, thus the generation of highly active nanoparticles.

Conflict of interest

There are no conflicts to declare.

Acknowledgements

The authors gratefully acknowledge financial support from SINOPEC Maoming Company, National Natural Science Foundation of China (21476145), and the Welch Foundation (V-0004).

References

1 J. E. Mondloch, E. Bayram and R. G. Finke, *J. Molecular Catal. A*, 2012, **355**, 1–38.
2 P. C. Stair, *J. Chem. Phys.*, 2008, **128**(182507), 1–4.
3 M. Campanati, G. Fornasari and A. Vaccari, *Catal. Today*, 2003, **77**, 299–314.
4 Y. Huang, Y. Li, P. Cheng, H. Chen, R. Li, X. Li, C. W. Yip and A. S. C. Chan, *J. Molecular Catal. A*, 2002, **189**, 219–224.
5 R. H. Crabtree, *Chem. Rev.*, 2012, **112**, 1536–1554.
6 A. Y. Khodakov, W. Chu and P. Fongarland, *Chem. Rev.*, 2007, **107**, 1692–1744.
7 C. K. Tsung, J. N. Kuhn, W. Huang, C. Aliaga, L. I. Hung, G. A. Somorjai and P. Yang, *J. Am. Chem. Soc.*, 2009, **131**, 5816–5822.
8 M. Cargnello, V. V. T. Doan-Nguyen, T. R. Gordon, R. E. Diaz, E. A. Stach, R. J. Gorte, P. Fornasiero and C. B. Murray, *Science*, 2013, **341**, 771–773.
9 R. Rinaldi, A. D. M. Porcari, T. C. R. Rocha, W. H. Cassinelli, R. U. Ribeiro, J. M. C. Bueno and D. Zanchet, *J. Molecul. Catal. A*, 2009, **301**, 11–17.
10 P. Li, J. Liu, N. Nag and P. A. Crozier, *Appl. Catal. A*, 2006, **307**, 212–221.
11 S. Lim, C. Wang, Y. Yang, D. Ciuparu, L. Pfefferle and G. L. Haller, *Catal. Today*, 2007, **123**, 122–132.
12 A. P. Wight and M. E. Davis, *Chem. Rev.*, 2002, **102**, 3589–3614.
13 A. T. Bell, *Science*, 2003, **299**, 1688–1691.
14 S. Kidambi, J. Dai, J. Li and M. L. Bruening, *J. Am. Chem. Soc.*, 2004, **126**, 2658–2659.
15 S. Bhattacharjee, D. M. Dotzauer and M. L. Bruening, *J. Am. Chem. Soc.*, 2009, **131**, 3601–3610.
16 T. Müller-Stach, A. Siani, T. Neubauer, X. Wei, US 20120077669A1.
17 L. Liu, S. Z. Luo, B. Wang and Z. Guo, *Appl. Surface Sci.*, 2015, **345**, 116–121.
18 J. Y. Oh, H. S. Choi, M. S. Kim, Y. S. Kim and C. R. Park, *J. Mater. Res.*, 2012, **27**, 2035–2045.
19 J. Graciani, K. Mudiyanselage, F. Xu, A. E. Baber, J. Evans, S. D. Senanayake, D. J. Stacchiola, P. Liu, J. Hrbek, J. F. Sanz and J. A. Rodriguez, *Science*, 2014, **345**, 546–550.
20 J. Gao, Q. Liu, F. Gu, B. Liu, Z. Zhong and F. Su, *RSC Adv.*, 2015, **5**, 22759–22776.
21 W. Wang, S. Wang, X. Ma and J. Gong, *Chem. Soc. Rev.*, 2011, **40**, 3703–3727.
22 S. Tada and R. Kukuchi, *Catal. Sci. Technol.*, 2015, **5**, 3061–3070.
23 F. Ocampo, B. Louis and A. C. Roger, *Appl. Catal. A*, 2009, **369**, 90–96.
24 M. A. Vannice, *J. Catal.*, 1982, **74**, 199–202.
25 T. Abe, M. Tanizawa, K. Watanabe and A. Taguchi, *Energy Environ. Sci.*, 2009, **2**, 315–321.
26 J. Sehested, S. Dahl, J. Jacobsen and J. R. Rostrup-Nielsen, *J. Phys Chem. B*, 2005, **109**, 2432–2438.
27 D. K. Beaman, E. J. Robertson and G. L. Richmond, *Langmuir*, 2012, **28**, 14245–14253.
28 W. Chu, P. A. Chernavskii, L. Gengembre, G. A. Pankina, P. Fongarland and A. Y. Khodakov, *J. Catal.*, 2007, **252**, 215–230.
29 P. G. J. de Gennes, *Chem. Phys.*, 1971, **55**, 572–579.
30 M. Doi and S. F. Edwards, *J. Chem. Soc. Faraday Trans.*, 1978, **274**, 1789–1801.
31 Z. F. Yan, R. G. Ding, L. H. Song and L. Qian, *Energy Fuels*, 1998, **12**, 1114–1120.
32 D. Hu, J. Gao, Y. Ping, L. Jia, P. Gunawan, Z. Zhong, G. Xu, F. Gu and F. Su, *Ind. Eng. Chem. Res.*, 2012, **51**, 4875–4886.
33 Z. Xu, N. Wang, W. Chu, J. Deng and S. Luo, *Catal. Sci. Technol.*, 2015, **5**, 1588–1597.
34 R. Razzaq, H. Zhu, L. Jiang, U. Muhammad, C. Li and S. Zhang, *Ind. Eng. Chem. Res.*, 2013, **52**, 2247–2256.
35 F. Ocampo, B. Louis and A. C. Roger, *Appl. Catal. A*, 2009, **369**, 90–96.
36 S. He, C. Li, H. Chen, D. Su, B. Zhang, X. Cao, B. Wang, M. Wei, D. G. Evans and X. Duan, *Chem. Mater.*, 2013, **25**, 1040–1046.
37 Y. Li, G. Lu and J. Ma, *RSC Adv.*, 2014, **4**, 17420–17428.
38 S. Tada, T. Shimizu, H. Kameyama, T. Haneda and R. Kikuchi, *Int. J. Hydrogen Energy*, 2012, **37**, 5527–5531.
39 J. Liu, C. Li, F. Wang, S. He, H. Chen, Y. Zhao, M. Wei, D. G. Evans and X. Duan, *Catal. Sci. Technol.*, 2013, **3**, 2627–2633.
40 M. C. J. Bradford and M. A. Vannice, *Catal. Rev.*, 1999, **41**, 1–42.
41 P. Zhou, S. Wang, C. Tao, X. Guo, L. Hao, Q. Shao, L. Liu, Y. P. Wang, W. Chu, B. Wang, S. Z. Luo and Z. Guo, *Adv. Polym. Technol.*, 2017, **36**, 1–11.